Journal of Atmospheric and Solar-Terrestrial Physics ▮ (▮▮▮▮) ▮▮▮–▮▮▮

Contents lists available at ScienceDirect

Journal of Atmospheric and Solar-Terrestrial Physics

journal homepage: www.elsevier.com/locate/jastp

Electric fields in the equatorial ionosphere derived from CHAMP satellite magnetic field measurements

Patrick Alken *, Stefan Maus

National Geophysical Data Center, NOAA E/GC1, 325 Broadway, Boulder, CO 80305-3328, USA

ARTICLE INFO

Article history:
Accepted 21 February 2009

Keywords:
Equatorial ionosphere
Electric fields
Equatorial electrojet
Modeling

ABSTRACT

The day-time eastward equatorial electric field (EEF) in the *E*-region plays an important role in equatorial ionospheric dynamics. It is responsible for driving the equatorial electrojet (EEJ) current system, equatorial vertical ion drifts, and the equatorial ionization anomaly (EIA). Due to its importance, there is much interest in accurately measuring the EEF. However, there is a severe lack of high quality data with the notable exception being the JULIA coherent scatter radar in Peru. In this work, we use CHAMP satellite-derived latitudinal current profiles of the day-time EEJ in order to estimate the eastward electric field at all longitudes, seasons, and day-side local times. We have constructed a dataset of over 32,000 EEF estimates based on six years of CHAMP data. Our estimates agree well with JULIA measurements, with an RMS difference of 0.13 mV/m.

1. Introduction

Neutral thermospheric winds in the equatorial region provide the energy required to maintain the zonal equatorial electric field (EEF). In the *E*-region, tidal winds drive currents to higher latitudes, which interact with the Earth's magnetic field, causing a buildup of positive and negative charges at the dawn and dusk terminators, respectively. This causes a strong eastward electric field on the equatorial day-side (Forbes, 1981; Heelis, 2004). This electric field is a primary driver of many ionospheric phenomena.

At the magnetic dip equator, the EEF drives a vertical Hall current and an eastward Pederson current. Since the upper and lower boundaries of the dynamo region are practically non-conducting, the Hall current is restricted, which leads to an enhanced eastward current flow known as the equatorial electrojet (EEJ) (Cowling, 1933). The EEJ is receiving renewed interest with the availability of large magnetic data sets from recent satellite missions. Magnetic signals of the EEJ current are an important tool to indirectly study the eastward electric field.

The EEF causes vertical $\mathbf{E} \times \mathbf{B}$ plasma drift upward at the dip equator. This vertical ion drift lifts equatorial plasma to altitudes above 800 km which then diffuses down magnetic field lines to form dense bands of plasma on either side of the magnetic equator at low latitudes (about 15° north and south of the dip equator). This is known as the equatorial ionospheric anomaly (EIA) (Appleton, 1954; Anderson, 1981). The vertical ion drift, whose velocity is $\mathbf{E} \times \mathbf{B}/B^2$ provides the opportunity to directly measure the EEF from Doppler shifts in radar echoes.

While the EEF is responsible for many important ionospheric processes, it has been difficult to measure or infer the electric field until recently. The JULIA (Jicamarca Unattended Long-term Investigations of the Ionosphere and Atmosphere) radar at the Jicamarca Radio Observatory has been measuring 150-km drift echoes, from which the EEF can be inferred, since 1996 (Hysell et al., 1997). While other radars have made similar measurements during various campaigns, JULIA is the only radar to have continuously measured the EEF over a long period of time. While the JULIA data have been used in many studies of the equatorial ionosphere (Fejer and Scherliess, 1997; Batista et al., 1996), they do not give a global picture of the EEF due to the fixed location of the observatory near Lima, Peru.

Recent satellite missions have for the first time made it possible to make global measurements of the EEF in all longitudes, local times, and seasons. Fejer et al. (2008) have constructed a global climatological vertical plasma drift model based on observations from the Ionospheric Plasma and Electrodynamics Probe Instrument (IPEI) aboard the ROCSAT-1 satellite, during the period from March 1999 to June 2004. Alken and Maus (2007) created a climatological model of the peak EEJ current based on magnetic field observations from the Ørsted and SAC-C satellites. While this model accurately predicts the climatology of the peak EEJ current, it does not take into account the full meridional structure of the EEJ current and therefore does not contain enough information to make estimates of the EEF.

In this study, we use the full latitudinal current structure of the EEJ current, as seen by the CHAMP satellite, to predict the eastward EEF for individual CHAMP equatorial passes. Previously,

* Corresponding author.
E-mail addresses: patrick.alken@noaa.gov (P. Alken), stefan.maus@noaa.gov (S. Maus).

1364-6826/$ - see front matter © 2009 Elsevier Ltd. All rights reserved.
doi:10.1016/j.jastp.2009.02.006

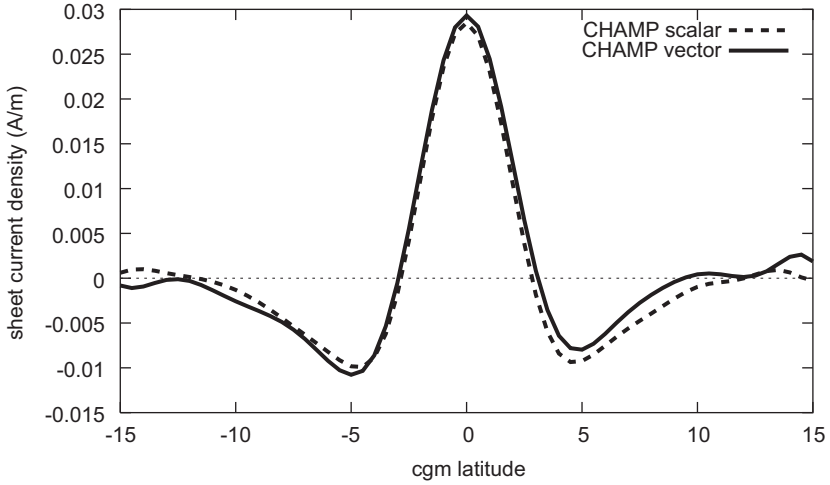

Fig. 1. Sample EEJ current profiles from CHAMP satellite scalar and vector magnetometer data.

Maus et al. (2007) studied CHAMP meridional current profiles averaged over all longitudes and seasons and attempted to estimate average electric field values as well as neutral wind profiles. They found difficulties, however, in separating the individual effects of the winds and the electric field. Alken et al. (2008) extended this work by using a much improved Horizontal Wind Model (HWM07). This eliminated the need to co-estimate the winds and therefore yielded more accurate electric field values for averaged CHAMP profiles. In this study, we extend this work to individual CHAMP passes, thereby creating a data set of over 32,000 EEF estimates at all longitudes, seasons and day-side local times during the years 2000 through 2006.

In Section 2 we discuss the CHAMP data used for this study. In Section 3 we describe our method of modeling the CHAMP EEJ meridional current profiles and the procedure of producing an electric field estimate. In Section 4 we compare the estimates with vertical drift measurements from the JULIA radar. In Section 5 we outline the main global features of the eastward electric field. Finally, in Section 6 we make some concluding remarks.

2. CHAMP data

The CHAMP satellite was launched into a polar circular orbit in July 2000 with an initial altitude of 454 km. Its mean altitude subsequently decayed to about 350 km by the end of 2006. The satellite completes an orbit every 92 min and decreases one hour in local time every eleven days. The instruments used in this study are the scalar magnetometer which measures the magnetic field intensity, and the vector magnetometer whose orientation in space is determined by a dual-head star camera.

Each time CHAMP flies over the dip equator on the day-side, it records a latitudinal magnetic profile from which the EEJ signature can be recovered (Lühr et al., 2004). First, the POMME-3.1 (Maus et al., 2006) model is subtracted which removes contributions from the core, mantle, crust and magnetosphere. The remaining residual magnetic signal is primarily due to the Sq current and the EEJ. To remove the Sq contribution, a background Sq signal was fitted outside a $\pm 12^\circ$ window around the dip equator and then subtracted to obtain a clean EEJ magnetic signal. To recover the current from the magnetic data, we inverted for parallel line currents at 108 km altitude with each line current representing 0.5° wide band of height integrated eastward current in corrected geomagnetic (cgm) coordinates (Richmond, 1995). Due to difficulties in separating the background magnetic field, there is some ambiguity in the zero level current. To overcome this problem, independent inversions of the scalar and vector data were done to validate a common zero level (Alken and Maus, 2007). These independent inversions are in good agreement, as shown in Fig. 1.

3. Modeling of EEJ current

The equations which govern the observed meridional CHAMP current profiles are (in geocentric spherical coordinates)

$$\nabla \times \mathbf{E} = 0 \tag{1}$$

$$\mathbf{J} = \nabla \times (\psi' \hat{\phi}) + J_\phi \hat{\phi} = \sigma(\mathbf{E} + \mathbf{u} \times \mathbf{B}) \tag{2}$$

where $\mathbf{E}$ is the electric field, $\mathbf{J}$ is the current density, ψ' is an unknown stream function to be determined, $\hat{\phi}$ is a unit vector in the eastward direction, σ is the conductivity tensor (Forbes, 1981, Eq. (10)), $\mathbf{u}$ is the neutral wind velocity, and $\mathbf{B}$ is the ambient magnetic field. Eq. (1) follows from Maxwell's steady state conditions and Eq. (2) follows from the steady state momentum equations (Forbes, 1981, pp. 479–480).

To model the current density $\mathbf{J}$, we first replace the unknown stream function ψ' with

$$\psi = -\psi' r \sin\theta \tag{3}$$

which will lead to simplifications in the resulting equations. Eq. (1) leads to

$$\left.\begin{aligned} \partial_\theta(\sin\theta E_\phi) &= 0 \\ \partial_r(rE_\phi) &= 0 \end{aligned}\right\} \Rightarrow E_\phi = \frac{RE_{\phi_0}}{r\sin\theta} \tag{4}$$

$$\partial_r(rE_\theta) - \partial_\theta(E_r) = 0 \tag{5}$$

where R is a constant of integration and acts as a reference radius, and E_{ϕ_0} is the equatorial eastward electric field at the radius R. Eq. (2) leads to

$$\frac{-1}{r^2\sin\theta}\partial_\theta\psi = \sigma_{rr}E_r + \sigma_{r\theta}E_\theta + \sigma_{r\phi}E_\phi + [\sigma(\mathbf{u}\times\mathbf{B})]_r \tag{6}$$

$$\frac{1}{r\sin\theta}\partial_r\psi = \sigma_{\theta r}E_r + \sigma_{\theta\theta}E_\theta + \sigma_{\theta\phi}E_\phi + [\sigma(\mathbf{u}\times\mathbf{B})]_\theta \tag{7}$$

$$J_\phi = [\sigma(\mathbf{E} + \mathbf{u}\times\mathbf{B})]_\phi \tag{8}$$

Once the unknown electric fields E_r and E_θ are found, Eq. (8) can be used to compute the eastward EEJ current as seen by CHAMP. Eliminating E_r and E_θ from Eqs. (5)–(7) yields a second order

Please cite this article as: Alken, P., Maus, S., Electric fields in the equatorial ionosphere derived from CHAMP satellite magnetic field measurements. Journal of Atmospheric and Solar-Terrestrial Physics (2009), doi:10.1016/j.jastp.2009.02.006

linear partial differential equation for the stream function ψ

$$\left[\frac{-1}{\alpha\sin\theta}\frac{\sigma_{rr}}{\sigma_{\theta r}}\right]\partial_r^2\psi+\left[\frac{1}{\gamma r^2\sin\theta}\right]\partial_\theta^2\psi + \left[\frac{1}{r\sin\theta}\left(\frac{1}{\gamma}\frac{\sigma_{r\theta}}{\sigma_{\theta\theta}}-\frac{1}{\alpha}\right)\right]\partial_r\partial_\theta\psi + \left[\frac{1}{r^2}\partial_\theta\left(\frac{1}{\gamma\sin\theta}\right)-\frac{1}{\sin\theta}\partial_r\left(\frac{1}{\alpha r}\right)\right]\partial_\theta\psi + \left[\frac{1}{r}\partial_\theta\left(\frac{1}{\gamma\sin\theta}\frac{\sigma_{r\theta}}{\sigma_{\theta\theta}}\right)-\frac{1}{\sin\theta}\partial_r\left(\frac{1}{\alpha}\frac{\sigma_{rr}}{\sigma_{\theta r}}\right)\right]\partial_r\psi + \partial_\theta\left(\frac{\delta}{\gamma}\right)-\partial_r\left(\frac{\beta r}{\alpha}\right)=0 \tag{9}$$

where

$$\alpha=\sigma_{r\theta}-\frac{\sigma_{rr}}{\sigma_{\theta r}}\sigma_{\theta\theta} \tag{10}$$

$$\beta=\left(\sigma_{r\phi}-\frac{\sigma_{rr}}{\sigma_{\theta r}}\sigma_{\theta\phi}\right)E_\phi+[\sigma(\mathbf{u}\times\mathbf{B})]_r - [\sigma(\mathbf{u}\times\mathbf{B})]_\theta\frac{\sigma_{rr}}{\sigma_{\theta r}} \tag{11}$$

$$\gamma=\sigma_{rr}-\frac{\sigma_{r\theta}}{\sigma_{\theta\theta}}\sigma_{\theta r} \tag{12}$$

$$\delta=\left(\sigma_{r\phi}-\frac{\sigma_{r\theta}}{\sigma_{\theta\theta}}\sigma_{\theta\phi}\right)E_\phi+[\sigma(\mathbf{u}\times\mathbf{B})]_r - [\sigma(\mathbf{u}\times\mathbf{B})]_\theta\frac{\sigma_{r\theta}}{\sigma_{\theta\theta}} \tag{13}$$

The expression used for the conductivity tensor σ is

$$\sigma=(\sigma_0-\sigma_p)\mathbf{b}\mathbf{b}^t+\sigma_p I_3+\sigma_h A \tag{14}$$

where σ_0, σ_p, and σ_h are the direct, Pederson, and Hall conductivities, respectively, $\mathbf{b}$ is a unit vector in the direction of the magnetic field $\mathbf{B}$, I_3 is the 3×3 identity matrix, and

$$A=\begin{pmatrix}0 & -b_\phi & b_\theta\\ b_\phi & 0 & -b_r\\ -b_\theta & b_r & 0\end{pmatrix} \tag{15}$$

b_r, b_θ, and b_ϕ are the radial, polar, and azimuthal components of $\mathbf{b}$, respectively. This expression follows directly from Richmond (1973, Eq. (1)). The equations used to compute the direct, Pederson and Hall conductivities can be found in Kelley (1989, Appendix B).

We solve Eq. (9) over a latitude range of -15 to 15° and an altitude range of 65–465 km, using finite differencing on a $0.25^\circ\times2$ km mesh with a nine cell stencil. For the boundary conditions, we require the stream function to vanish at the upper and lower boundaries, and its normal derivative to vanish at the northern and southern boundaries. The resulting matrix equation is solved with a sparse matrix algorithm. For the conductivity inputs to this equation, we use the International Reference Ionosphere IRI-2007 to obtain the ion and electron densities and temperatures. The neutral densities are taken from the thermospheric model NRLMSISE-00 (Picone et al., 2002). The neutral winds $\mathbf{u}$ are taken from the provisional Horizontal Wind Model HWM07 (John Emmert, Douglas Drob, personal communication), which provides zonal and meridional wind information. In a previous study, Alken et al. (2008) found that HWM07 leads to much improved accuracy in modeling averaged EEJ current profiles, compared to the older HWM93 model, but they only included zonal winds in their study. Here we also include meridional wind effects, though they are thought to be small (Hysell et al., 2002). Vertical wind effects are not included in this study. The ambient geomagnetic field $\mathbf{B}$ is taken from the POMME main field model (Maus et al., 2006). The eastward electric field E_{ϕ_0} is assumed constant over the region of integration and is initially taken to be 1 mV/m.

After the PDE in Eq. (9) is solved, the electric fields E_r and E_θ can be recovered using Eqs. (6) and (7). Finally, the eastward EEJ current J_ϕ corresponding to our eastward electric field input E_{ϕ_0} can be calculated using Eq. (8). Once J_ϕ has been computed, it can be compared with the corresponding CHAMP current profile to estimate the eastward electric field. To accomplish this, a scaling factor s is computed to minimize the error between $J_{PDE}(sE_{\phi_0})$ and J_{CHAMP}, where J_{PDE} is the J_ϕ solution from the PDE, height integrated from 65 to 465 km, and J_{CHAMP} is the corresponding CHAMP meridional current profile. The electric field estimate is given by sE_{ϕ_0}. In order to eliminate the need to re-solve the PDE for each choice of s, we note that

$$J_{PDE}(sE_{\phi_0})=sJ_{PDE}(E_{\phi_0}) \tag{16}$$

provided that the wind input $\mathbf{u}$ is zero. Since all of the equations are linear, we can use

$$J_{PDE}(E_{\phi_0},\mathbf{u})=J_{PDE}(E_{\phi_0},\mathbf{u}=0)+J_{PDE}(E_{\phi_0}=0,\mathbf{u}) \tag{17}$$

which allows us to set up the CHAMP inversion as

$$J_{CHAMP}=sJ_{PDE}(E_{\phi_0},\mathbf{u}=0)+J_{PDE}(E_{\phi_0}=0,\mathbf{u})-J_{DC} \tag{18}$$

where the parameters to be optimized are the scaling factor s and a possible DC offset J_{DC}.

The PDE in Eq. (9) is solved twice for each CHAMP profile, once with the wind input set to 0, and once with the eastward electric field input set to 0. The CHAMP profile inversion in Eq. (18) is performed by a least squares method where the parameters s and J_{DC} are constrained to make the PDE and CHAMP profiles agree at the magnetic equator. This is done because the value of the eastward current at the magnetic equator is primarily due to the eastward electric field, while the winds have more of an effect off of the equator (Fambitakoye et al., 1976, Figs. 1 and 2). The most accurate electric field estimate is obtained by constraining the PDE solution to agree with CHAMP at the magnetic equator, verified by comparing exact overflights with the JULIA radar (see below). There may be some errors introduced with this procedure in some longitude sectors since the CHAMP current profiles were computed in cgm coordinates but we solve our PDE in geocentric coordinates. In a follow-on study we plan to extend our modeling to cgm coordinates to eliminate any possible errors arising from this.

Some sample individual CHAMP profiles along with their corresponding modeled solutions are shown in Fig. 2. These profiles include the $4v_e$ correction which is described in more detail below. The majority of modeled profiles agree well with their CHAMP counterparts. Sixty percent of the modeled profiles had a correlation with CHAMP of above 0.7. Of those profiles with poor correlations, some were taken during the evening when the EEJ current signal is very small, causing errors to amplify. Some are simply the result of the difficulties in modeling day to day highly variable data, especially since our conductivity and wind models are climatological.

4. Comparison with JULIA vertical drift measurements

To verify our method of modeling the EEF, we compare our results with the vertical drift measurements of the JULIA radar. JULIA is a coherent scatter radar data acquisition system located at the Jicamarca Radio Observatory (11.95°S, 76.87°W), which makes high quality measurements of 150-km drift echoes.

Please cite this article as: Alken, P., Maus, S., Electric fields in the equatorial ionosphere derived from CHAMP satellite magnetic field measurements. Journal of Atmospheric and Solar-Terrestrial Physics (2009), doi:10.1016/j.jastp.2009.02.006

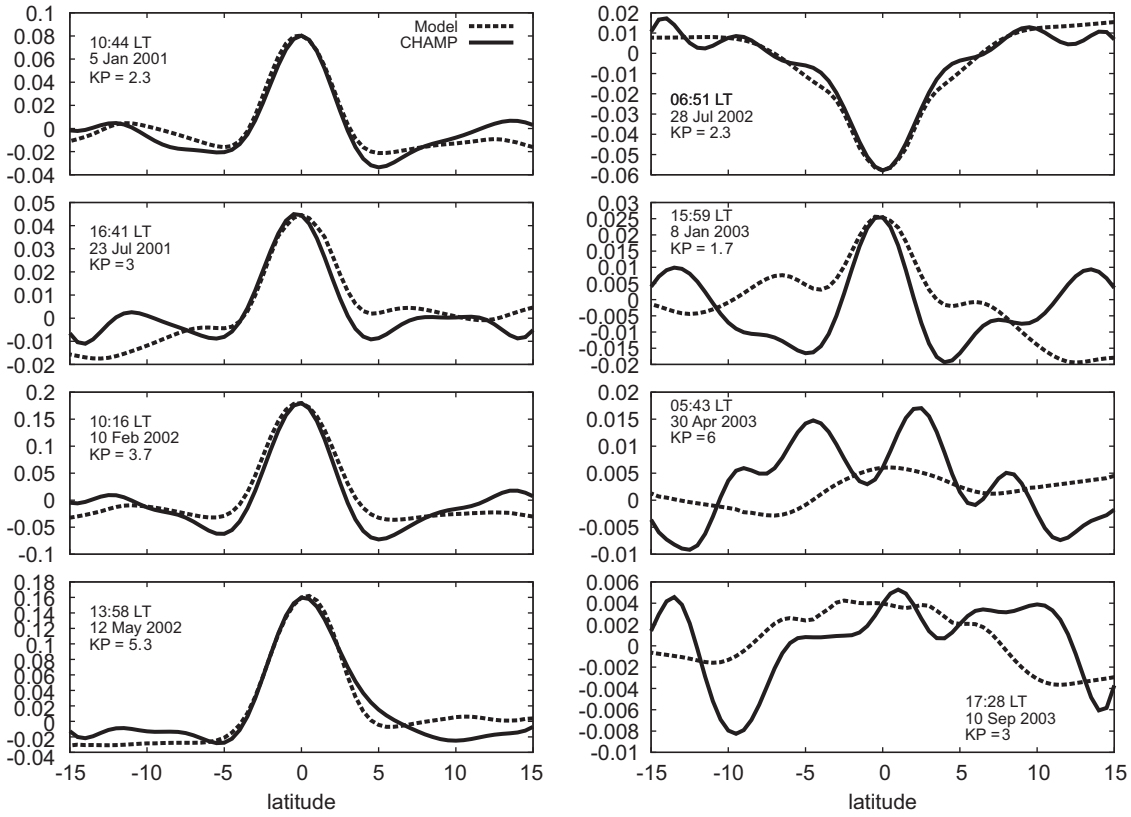

Fig. 2. A random sample of individual CHAMP current profiles (solid) with the corresponding modeled profiles (dotted).

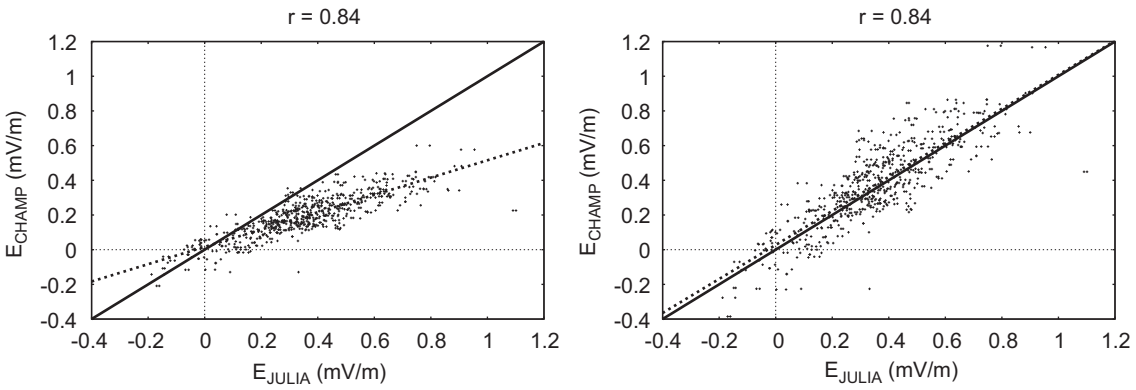

Fig. 3. Comparison of electric field estimates from CHAMP with electric field measurements from the JULIA radar. Best fit line is dotted, $y = x$ line is solid. Left: CHAMP estimates using unmodified electron collision frequency from NRLMSISE-00 and IRI2007 models. Best fit line: $E_{CHAMP} = 0.50 \times E_{JULIA} + 0.02$. Right: CHAMP estimates using electron collision frequency enhanced by a factor of 4. Best fit line: $E_{CHAMP} = 0.98 \times E_{JULIA} + 0.03$.

Upon initially comparing the results of our modeling process with the JULIA data, we found that the CHAMP electric field values systematically underestimated JULIA EEF estimates by about a factor of 2. Gagnepain et al. (1977) found when comparing early EEJ models that the observed value of the electron collision frequency had to be multiplied by a factor of 4 in order to produce results which accurately reflected observed parameters of the EEJ. Ronchi et al. (1990) then put this ad hoc assumption on a firmer theoretical footing by demonstrating that the inclusion of small scale turbulence effects on the larger scale plasma dynamics, which were not previously taken into account, enhances the electron Pederson mobility and reduces the polarization electric field. These effects can be modeled by increasing the observed electron collision frequency.

In this study, we adopted the convention of increasing the electron collision frequency (as computed by the NRLMSISE-00 and IRI2007 models) by a factor of 4. This method is also utilized by the TIEGCM model in simulations of the EEJ (Fang et al., 2008). The resulting zonal electric field estimates from CHAMP are in impressive agreement with the electric field measurements from JULIA, as shown in Fig. 3. As can be seen, the CHAMP eastward electric field estimates are drastically improved with the higher electron collision frequency. These plots were generated from all available JULIA and CHAMP data from 1 August 2001 to 26 November 2006. Data were selected in the local time sector 0700–1600 LT and whenever CHAMP passed within 10° longitude of the JULIA radar location. These criteria led to 628 CHAMP equatorial crossings. Fig. 3 shows data for all values of *Kp*,

Please cite this article as: Alken, P., Maus, S., Electric fields in the equatorial ionosphere derived from CHAMP satellite magnetic field measurements. Journal of Atmospheric and Solar-Terrestrial Physics (2009), doi:10.1016/j.jastp.2009.02.006

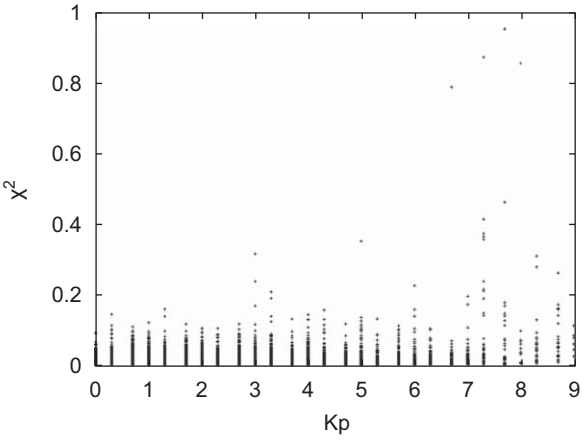

Fig. 4. Misfit between CHAMP current profiles and corresponding modeled profiles as a function of *Kp*.

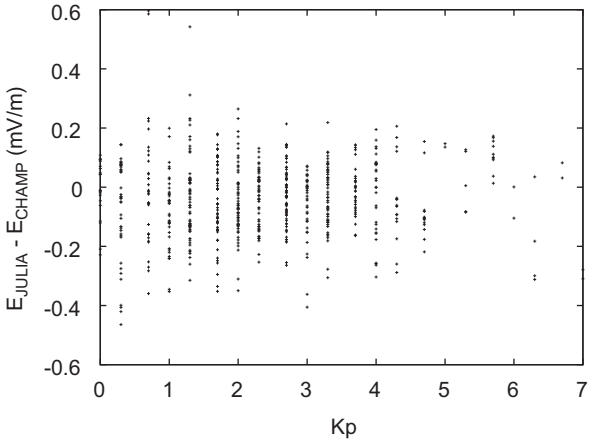

Fig. 5. Difference between CHAMP electric field estimates and corresponding JULIA data as a function of *Kp*.

providing some confirmation that our modeling process yields accurate electric field estimates during both quiet and disturbed times. We find a correlation coefficient of 0.84 for both the original and modified electron collision frequencies. With the modified collision frequency, the slope of the best fit line remarkably improved to 0.98, close to the ideal value of 1.0, indicating that our modeled electric field values agree well with the JULIA data. The RMS difference between the CHAMP electric field estimates and JULIA values is 0.13 mV/m. While the $4v_e$ correction produces very accurate results in the Peruvian sector, the validity of this adjustment at other longitudes still needs to be verified. All subsequent figures in this paper include the $4v_e$ correction.

To further investigate the sensitivity of our modeling procedure to *Kp*, we show in Fig. 4 the error χ^2 between the CHAMP profiles and their corresponding modeled profiles as a function of *Kp*. The misfit function is defined as

$$\chi^2 = \sum_i [J_{CHAMP}(\theta_i) - J_{PDE}(\theta_i)]^2 \tag{19}$$

where the sum is taken over the latitude range -15 to 15°, and the term J_{PDE} is the full modeled solution, using the optimized eastward electric field value, wind contributions and *DC* offset. Remarkably the maximum misfit between the observed and modeled profiles remains relatively constant except for a few disturbed profiles in the range $7 \leqslant Kp \leqslant 9$.

It is also instructive to compare our electric field measurements directly with JULIA as a function of *Kp*. This is shown in Fig. 5. Again we used all available CHAMP passes over the JULIA radar within $\pm 10^\circ$. We see that the difference between the JULIA electric field values and the CHAMP estimates does not significantly increase with *Kp*.

A further important consideration is how daily departures of ionospheric and thermospheric parameters from the climatological mean given by the IRI2007 and NRLMSISE-00 models may affect our electric field estimates, since the conductivity tensor σ is computed entirely from these two models. We examined a single CHAMP current profile and varied the relevant IRI and MSIS parameters to determine the corresponding uncertainties in the electric field estimate. Varying the electron temperature by $\pm 50\%$ leads to about a $\pm 10\%$ change in the electric field estimate. Increasing the electron density from IRI by 50% leads to a -20% change in the EEF estimate, while decreasing it by 50% leads to a $+47\%$ change. Changing the electron collision frequency by $\pm 50\%$ (before the factor 4 correction) leads to a change of about 30% in the EEF estimate. Changing the ion collision frequencies by $\pm 50\%$ leads to a maximum change in the estimate by about 30%. The neutral densities obtained from MSIS lead to less than a 5% difference in the EEF estimate when varied by $\pm 50\%$. It is remarkable that errors in the neutral density model have such a small effect on our EEF estimate and so we conclude that the main source of error in our conductivity will come from the IRI model, especially in the calculation of the electron/ion densities.

We also considered departures of the daily wind field from the Horizontal Wind Model, and their effects on our EEF estimates. We examined the effects of the zonal and meridional winds separately, and scaled the winds by a constant factor at all altitudes of interest. When scaling the zonal winds by $\pm 50\%$ at all altitudes, we find a difference of $\pm 17\%$ in the EEF estimate. The meridional winds had a much smaller effect, as expected. Scaling these winds by $\pm 50\%$ at all altitudes leads to less than a 1% difference in the EEF estimate. The storm time component of the Horizontal Wind Model was not included in this study. In a future study we plan to include disturbance wind effects which may help to further reduce errors during storm-time conditions.

5. Global features of the eastward electric field

In Fig. 6 we plot the eastward electric field estimates as a function of longitude and local time for all four seasons during quiet-time ($Kp \leqslant 3$). During equinox and June solstice we see the well known wavenumber-4 structure as well as the wavenumber-3 structure during December solstice. The wavenumber-4 longitudinal structure has been observed in many different data sets. England et al. (2006) found a wavenumber-4 structure in the peak noon-time EEJ current values derived from the CHAMP, SAC-C and Ørsted satellites. Alken and Maus (2007) later constructed a climatological model of the peak EEJ current densities which clearly exhibits a wave-4 structure during equinox and June solstice, as well as a wave-3 structure during December solstice. Hartman and Heelis (2007) also found a wavenumber-4 structure in equatorial vertical ion drift measurements of the DMSP satellite (830 km altitude) in the 0930 local time sector during September. Fejer et al. (2008) recently constructed a climatological vertical plasma drift model from ROCSAT-1 measurements which also exhibits the wave-4 and wave-3 structures at different seasons.

Recent studies attribute the wavenumber-4 longitudinal pattern to the eastward propagating diurnal tide with zonal wavenumber-3 (DE3) originating in the tropical troposphere. Lühr et al. (2008) performed a detailed analysis of the effects of DE3 on the EEJ using the climatological model EEJM-1 of Alken and Maus (2007). They found that DE3 is the primary contributor to

Please cite this article as: Alken, P., Maus, S., Electric fields in the equatorial ionosphere derived from CHAMP satellite magnetic field measurements. Journal of Atmospheric and Solar-Terrestrial Physics (2009), doi:10.1016/j.jastp.2009.02.006

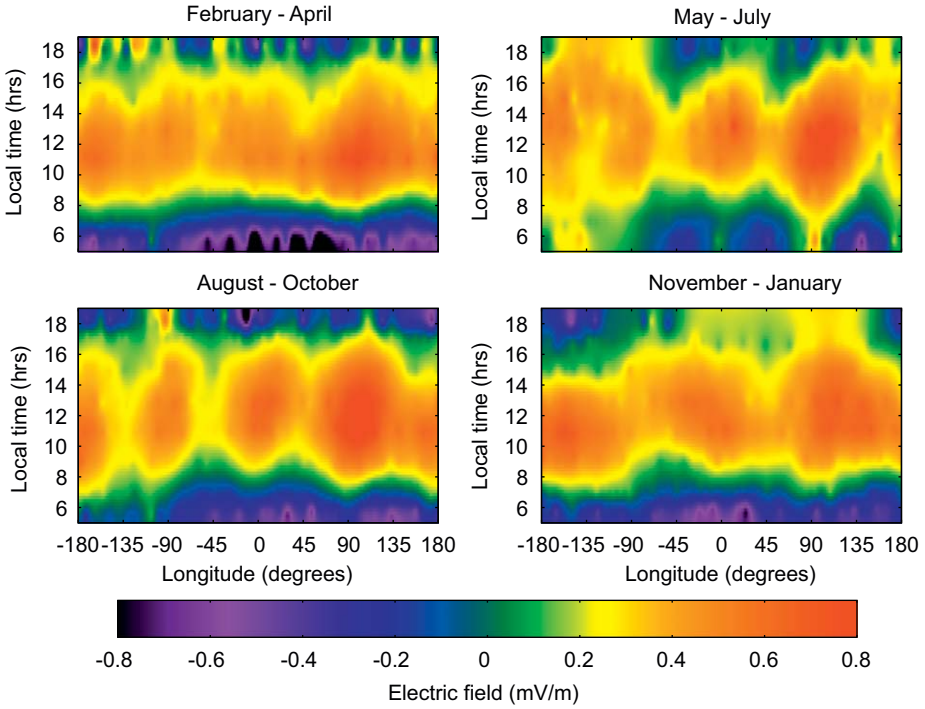

Fig. 6. Electric field as a function of longitude and local time for different seasons at low Kp ($\leqslant 3$).

longitudinal variations in the EEJ, especially during the months April–October.

We find longitudinal peaks during both equinoxes near −170°, −90°, 0°, and 100° longitude, in agreement with the findings of Alken and Maus (2007) and Fejer et al. (2008). Also significant is the strength of the EEF during September equinox as compared to March equinox. This feature is also seen in the magnetic data from CHAMP but was not incorporated into the seasonal dependence in the model of Alken and Maus (2007). During December solstice we see peaks near −170°, 0° and 100° also in agreement with Fejer et al. (2008). In June solstice we find a large peak near 100°, a much smaller peak near 10° and a broad peak in the longitudinal sector −180° to −90° which appears as a double peak during the 0800–1400 local time sector, and appears as a single peak in the early morning and the evening, also in agreement with the findings of Fejer et al. (2008).

In Fig. 7 we plot the electric field as a function of longitude and season around 1200 LT for quiet-time ($Kp \leqslant 3$). Here we see that the electric field is strongest during September equinox, especially at the 100° peak. The peak at −170° tends to be stronger closer to December solstice and into January. The peak at −170° appears to drift to around −150° during December solstice leading to the wave-3 structure we observe. The seasonal dependence of the electric field is further illustrated in Fig. 8 where we plot the raw data for the 1100–1300 local time sector near the longitudes −170° and 100°, along with a smoothed data curve. Here we see a large peak during September equinox in the 80–110° longitude sector with smaller peaks during January, March equinox, May, July, and December solstice. In the −180 to −160° longitude sector, we find stronger peaks in January and March equinox with four smaller peaks during May, July, September equinox and November. Though our data appears to exhibit a six peak structure in season, some of these features may be caused by a lack of CHAMP data at all seasons near 1200 LT, and further study is required to determine if these features are physically real.

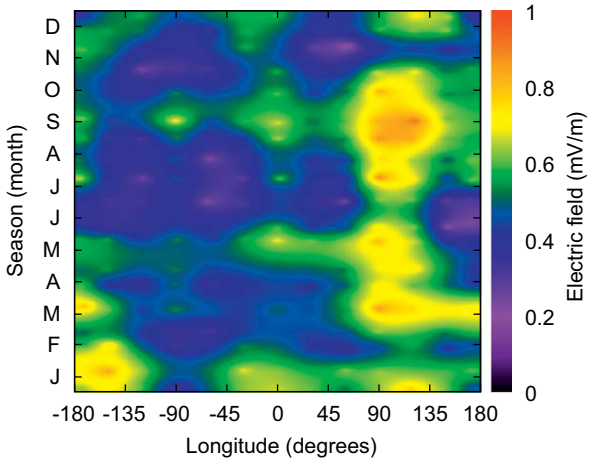

Fig. 7. Electric field as a function of longitude and season for 1100–1300 local time at low Kp ($\leqslant 3$).

In Fig. 9 we plot the eastward electric field as a function of local time and season for the longitudinal peak near 100°. We find that the EEF has a broad peak in the 1000–1400 local time sector during all seasons. We again see multiple seasonal peaks in the data, especially around local noon, but again we caution this could be due to noise or an insufficient amount of data.

We show a clearer picture of the local time dependence in Fig. 10. Here we plot our raw electric field estimates as a function of local time during September equinox with a smoothed data curve. In the upper plot we display the peak occurring at 100° by taking all data in the longitude sector 80–110°. The bottom plot represents the peak occurring near 0° by taking data in the longitude sector −10–20°. In both cases we see a westward electric field in the early morning hours and a steady rise to a

Please cite this article as: Alken, P., Maus, S., Electric fields in the equatorial ionosphere derived from CHAMP satellite magnetic field measurements. Journal of Atmospheric and Solar-Terrestrial Physics (2009), doi:10.1016/j.jastp.2009.02.006

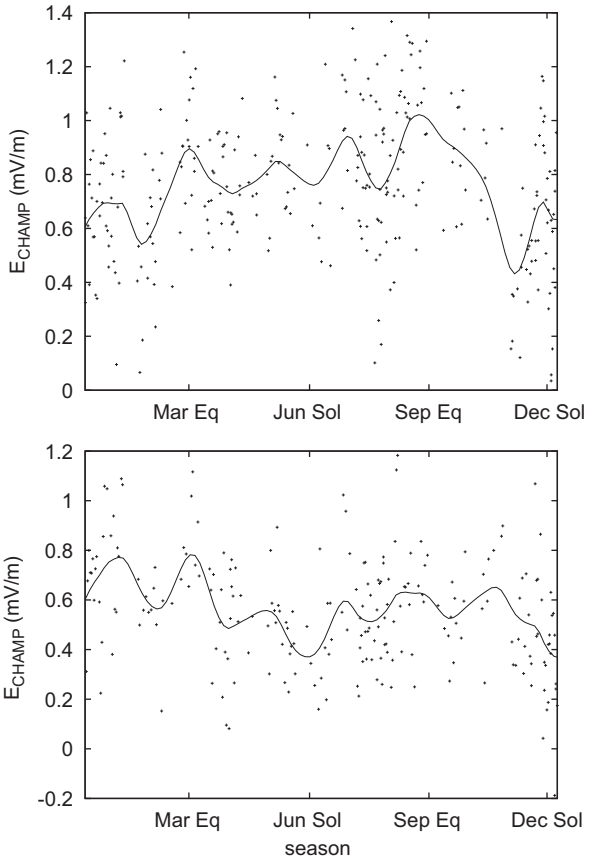

Fig. 8. Electric field as a function of season for 1100–1300 local time at low *Kp* ($\leqslant 3$). Top: all data for the longitude sector 80–110°. Bottom: all data for the longitude sector −180 to −160°. The solid curve in both plots represents a smoothing of the data by Tikhonov regularization.

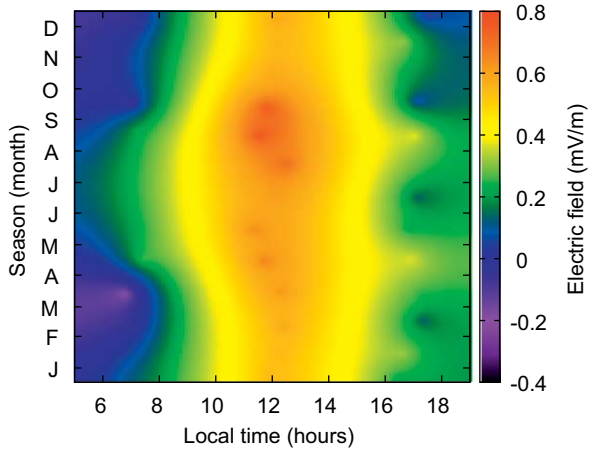

Fig. 9. Electric field as a function of local time and season for 80–110° longitude at low *Kp* ($\leqslant 3$).

broad peak around 1000–1400 LT. The electric field then steadily decreases to zero at about 1800 LT.

6. Discussion

We have successfully implemented a procedure to solve the differential equations governing the EEJ in conjunction with observed CHAMP satellite meridional EEJ current profiles to produce estimates of the eastward electric field. We have constructed a data set of over 32,000 electric field estimates with coverage of all longitudes, seasons, and day-time local times. Our estimates were compared with vertical drift measurements from the JULIA coherent scatter radar at Jicamarca, Peru, finding a high correlation of 0.84 as well as a best fit slope of 0.98 between the JULIA electric field measurements and our estimates based on CHAMP. Our analysis has been carried out during both quiet and disturbed times, and we find good agreement with JULIA even during highly disturbed times. The RMS difference between the JULIA and CHAMP-derived electric field values is 0.13 mV/m. For this error estimate, no data were excluded for any reason.

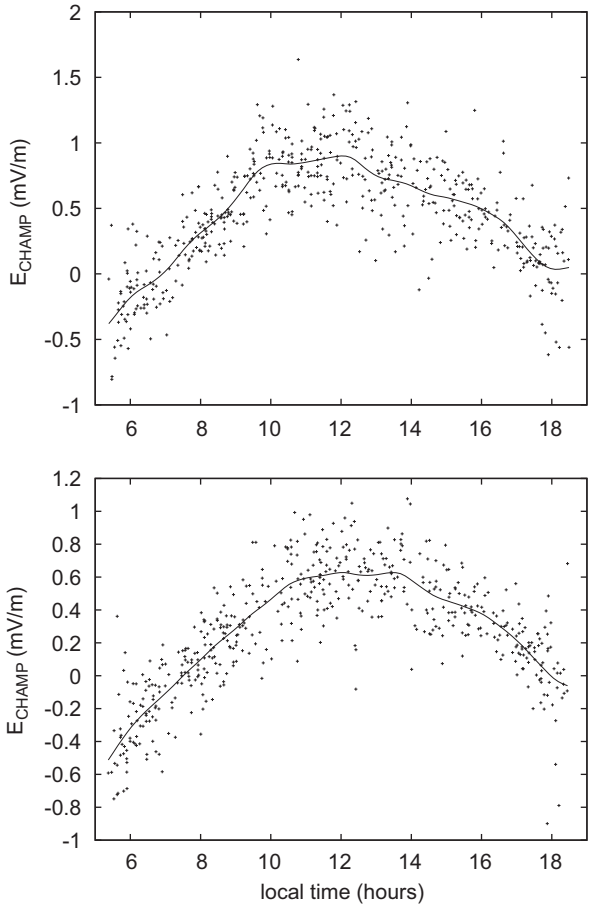

Fig. 10. Electric field as a function of local time during September equinox at low *Kp* ($\leqslant 3$). Top: all data for the longitude sector 80–110°. Bottom: all data for the longitude sector −10–20°. The solid curve in both plots represents a smoothing of the data by Tikhonov regularization.

We have shown that our electric field estimates exhibit previously identified behavior in longitude, local time, and season. We find the well known wave-4 and wave-3 longitudinal structures at different seasons in agreement with several previous studies (England et al., 2006; Alken et al., 2008). Seasonally, we find peaks in the EEF during equinox at most longitudes as well as a much stronger field during September equinox compared to March equinox. In local time, we find a westward electric field in the early morning and a broad peak in the EEF around 1000–1400 LT.

We have examined the effects of errors in the IRI-2007, NRLMSISE-00 and HWM07 models on our EEF estimates. We find that the largest changes in our EEF estimates will come from daily variations in the electron/ion densities, the electron/ion collision

Please cite this article as: Alken, P., Maus, S., Electric fields in the equatorial ionosphere derived from CHAMP satellite magnetic field measurements. Journal of Atmospheric and Solar-Terrestrial Physics (2009), doi:10.1016/j.jastp.2009.02.006

frequencies, and the zonal winds. Variations in the electron temperature, neutral densities, and meridional winds have very little effect on the EEF estimates. In all cases, uncertainties in ionospheric and thermospheric parameters lead to a smaller corresponding effect on the electric field estimates as required for a reliable modeling method.

As mentioned before, vertical wind effects were not included in this study. Vertical winds can have a substantial effect on vertical polarization electric fields and consequently the zonal electric field in the *E*-region (Hysell et al., 2002). Anandarao et al. (1978) report up to 20 m/s vertical winds in the equatorial region at altitudes of 95–100 km. These winds could have large effects on the EEJ, and possibly even cause counter-electrojet conditions (Raghavarao and Anandarao, 1980). Unfortunately very few studies exist on vertical wind effects at the equator, and those that do normally have data for only a few heights and rely on considerable extrapolation (Anandarao et al., 1978). Therefore, due to a lack of data and models, we are unable to include vertical wind effects in our present study.

Overall we believe our method to be a significant advance in the study of equatorial electrodynamics. This work will open possibilities for future studies into the climatology of the EEF, studies of the EEF during disturbed times, as well as the study of the many ionospheric phenomena influenced by the EEF.

Acknowledgment

The operational support of the CHAMP mission by the German Aerospace Center (DLR) is gratefully acknowledged.

References

Alken, P., Maus, S., 2007. Spatio-temporal characterization of the equatorial electrojet from CHAMP, Ørsted, and SAC-C satellite magnetic measurements. J. Geophys. Res. 112.

Alken, P., Maus, S., Emmert, J., Drob, D.P., 2008. Improved horizontal wind model HWM07 enables estimation of equatorial ionospheric electric fields from satellite magnetic measurements. Geophys. Res. Lett. 35.

Anandarao, B.G., Raghavarao, R., Desai, J.N., Haerendel, G., 1978. Vertical winds and turbulence over Thumba. J. Atmos. Terr. Phys. 40, 157–159.

Anderson, D.N., 1981. Modeling the ambient, low latitude F-region ionosphere—a review. J. Atmos. Terr. Phys. 43 (8), 753–762.

Appleton, E.V., 1954. The anomalous equatorial belt in the F2-layer. J. Atmos. Terr. Phys. 5, 348.

Batista, I.S., Medeiros, R.T., Abdu, M.A., deSouza, J.R., Bailey, G.J., dePaula, E.R., 1996. Equatorial ionospheric vertical plasma drift model for the Brazilian region. J. Geophys. Res. 101, 10887–10892.

Cowling, T.G., 1933. The electrical conductivity of an ionized gas in the presence of a magnetic field. Mon. Not. R. Astron. Soc. 93, 90–98.

England, S.L., Maus, S., Immel, T.J., Mende, S.B., 2006. Longitudinal variation of the E-region electric fields caused by atmospheric tides. Geophys. Res. Lett. 33.

Fambitakoye, O., Mayaud, P.N., Richmond, A.D., 1976. The equatorial electrojet and regular daily variation S_R:-III. Comparison of observations with a physical model. J. Atmos. Terr. Phys. 38, 113–121.

Fang, T.W., Richmond, A.D., Liu, J.Y., Maute, A., Lin, C.H., Chen, C.H., Harper, B., 2008. Model simulation of the equatorial electrojet in the Peruvian and Phillipine sectors. J. Atmos. Sol. Terr. Phys. 70, 2203–2211.

Fejer, B.G., Jensen, J.W., Su, S.-Y., 2008. Quiet-time equatorial *F* region vertical plasma drift model derived from ROCSAT-1 observations. J. Geophys. Res. 113.

Fejer, B.G., Scherliess, L., 1997. Empirical models of storm time equatorial zonal electric fields. J. Geophys. Res. 102 (A11), 24047–24056.

Forbes, J.M., 1981. The equatorial electrojet. Rev. Geophys. Space Phys. 19 (3), 469–504.

Gagnepain, J., Crochet, M., Richmond, A.D., 1977. Comparison of equatorial electrojet models. J. Atmos. Terr. Phys. 39, 1119–1124.

Hartman, W.A., Heelis, R.A., 2007. Longitudinal variations in the equatorial vertical drift in the topside ionosphere. J. Geophys. Res. 112 (A03305).

Heelis, R.A., 2004. Electrodynamics in the low and middle latitude ionosphere: a tutorial. J. Atmos. Sol. Terr. Phys. 66, 825–838.

Hysell, D.L., Chau, J.L., Fesen, C.G., 2002. Effects of large horizontal winds on the equatorial electrojet. J. Geophys. Res. 107 (A8).

Hysell, D.L., Larsen, M.F., Woodman, R.F., 1997. JULIA radar studies of electric fields in the equatorial electrojet. Geophys. Res. Lett. 24 (13), 1687–1690.

Kelley, M.C., 1989. The Earth's Ionosphere: Plasma Physics and Electrodynamics. Academic Press Inc., San Diego.

Lühr, H., Maus, S., Rother, M., 2004. Noon-time equatorial electrojet: its spatial features as determined by the CHAMP satellite. J. Geophys. Res. 109.

Lühr, H., Rother, M., Häusler, K., Alken, P., Maus, S., 2008. The influence of non-migrating tides on the longitudinal variation of the equatorial electrojet. J. Geophys. Res. 113.

Maus, S., Alken, P., Lühr, H., 2007. Electric fields and zonal winds in the equatorial ionosphere inferred from CHAMP satellite magnetic measurements. Geophys. Res. Lett. 34.

Maus, S., Rother, M., Stolle, C., Mai, W., Choi, S., Lühr, H., Cooke, D., Roth, C., 2006. Third generation of the Potsdam magnetic model of the earth (POMME). Geochem. Geophys. Geosyst. 7.

Picone, J.M., Hedin, A.E., Drob, D.P., Aikin, A.C., 2002. NRLMSISE-00 empirical model of the atmosphere: statistical comparisons and scientific issues. J. Geophys. Res. 107.

Raghavarao, R., Anandarao, B.G., 1980. Vertical winds as a plausible cause for equatorial counter electrojet. Geophys. Res. Lett. 7, 357.

Richmond, A.D., 1973. Equatorial electrojet—I. Development of a model including winds and electric field. J. Atmos. Terr. Phys. 35, 1083–1103.

Richmond, A.D., 1995. Ionospheric electrodynamics using magnetic apex coordinates. J. Geomagn. Geoelectr. 47, 191–212.

Ronchi, C., Sudan, R.N., Similon, P.L., 1990. Effect of short-scale turbulence on kilometer wavelength irregularities in the equatorial electrojet. J. Geophys. Res. 95 (A1), 189–200.

Please cite this article as: Alken, P., Maus, S., Electric fields in the equatorial ionosphere derived from CHAMP satellite magnetic field measurements. Journal of Atmospheric and Solar-Terrestrial Physics (2009), doi:10.1016/j.jastp.2009.02.006